Integrated Aeromechanics with Three-Dimensional Solid-Multibody Structures

Anubhav Datta
Science and Technology Corp
AFDD at Ames Research Center
Moffett Field, CA 94035

Wayne Johnson
Aeromechanics Branch
NASA Ames Research Center
Moffett Field, CA 94035

ABSTRACT

A full three-dimensional finite element-multibody structural dynamic solver is coupled to a three-dimensional Reynolds-averaged Navier-Stokes solver for the prediction of integrated aeromechanical stresses and strains on a rotor blade in forward flight. The objective is to lay the foundations of all major pieces of an integrated three-dimensional rotor dynamic analysis — from model construction to aeromechanical solution to stress/strain calculation. The primary focus is on the aeromechanical solution. Two types of three-dimensional CFD/CSD interfaces are constructed for this purpose with an emphasis on resolving errors from geometry mis-match so that initial-stage approximate structural geometries can also be effectively analyzed. A three-dimensional structural model is constructed as an approximation to a UH-60A-like fully articulated rotor. The aerodynamic model is identical to the UH-60A rotor. For preliminary validation measurements from a UH-60A high speed flight is used where CFD coupling is essential to capture the advancing side tip transonic effects. The key conclusion is that an integrated aeromechanical analysis is indeed possible with three-dimensional structural dynamics but requires a careful description of its geometry and discretization of its parts.

INTRODUCTION

The objective of this paper is to lay the foundations of an integrated three-dimensional (3D) aeromechanical analysis for helicopter rotors. The words "integrated 3D aeromechanics" are used to mean three-dimensional structural dynamics coupled to three-dimensional fluid dynamics for the prediction of dynamic stresses and strains with an equal fidelity of representation in structures and fluids.

The state of the art in aeromechanical analysis uses Reynolds Averaged Navier-Stokes (RANS) based Computational Fluid Dynamics (CFD) containing tens of millions of grid points on hundreds of cores, routinely, in a research environment for the rotor, and even for the entire helicopter. Arbitrary blade contours, aircraft configurations, and flight conditions can be analyzed effectively from first principles. Computations in the structural domain continue to use engineering-level beam-multibody models that are historically part of lifting-line comprehensive codes carried out on a single processor [1]. Thus the high-fidelity CFD airloads are not directly integrated with stress/strain calculations. Similarly detailed finite element stress analysis is performed routinely on structures but only on isolated components with loading from beam analysis or previous flight test data. Thus high-fidelity structures is not integrated with high-fidelity airloads. The need for high-fidelity structures for dynamics is clear. Modern rotors contain flexible components near the hub that provide the critical couplings for dynamics and encounter the critical stresses. These have short aspect ratios, open sections, and end constraints, and cannot be treated as beams. Blades envisioned with advanced shapes and the ability to morph in flight cannot be treated from first principles using beams.

The broad objective of this research is to close this gap by developing a scalable 3D solid-multibody based Computational Structural Dynamics (CSD) solver. The formulations for 3D scalability and multibody dynamics were covered earlier in Refs [2] and [3]. The focus of this paper is on integrated aeromechanics. The specific objectives are: 1. to develop a 3D CFD/CSD coupled solution procedure and demonstrate it on a realistic articulated rotor and 2. to implement an entire 3D workflow from model construction to aeromechanical solution to stress/strain calculation.

Presented at the American Helicopter Society 70th Annual Forum, Montréal, Québec, May 20–22, 2014.

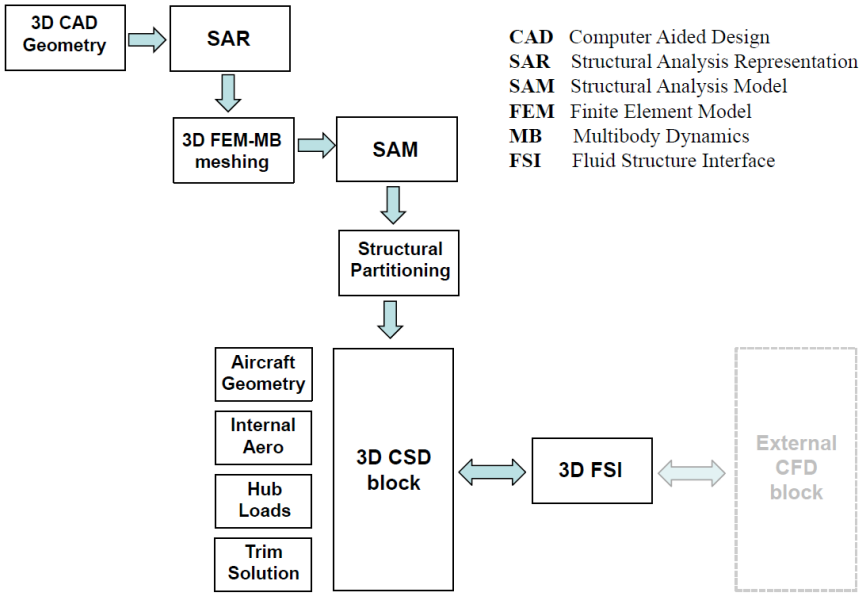

Figure 1: **Integrated 3D workflow.**

The field of computational 3D fluid-structure interaction is vast and varied (see recent reviews and texts [4]– [8]) but have never been applied in the context of rotorcraft. Rotorcraft requires a special solution procedure — a straight forward exchange of states and accompanying iterations will not do. Rotor control angles must be simultaneously determined to satisfy the aircraft trim state. Adequate aerodynamic damping must be provided to the structure as a pre-conditioner so that all classes of rotors can be solved. Theoretical considerations of conservation and consistency are not sufficient, an effective analysis must accommodate early-stage structural descriptions with significant geometry mis-match. These are the particular emphases of this paper.

The 3D structural model constructed for this work is an idealized representation of a fully articulated UH-60A-like rotor. Construction of exact geometries from CAD and generation of 3D finite element-multibody meshes is a separate dedicated effort in itself and described in a companion paper [9].

Scope and Organization of Paper

The main emphasis of this work is on the development and demonstration of an integrated 3D CFD/CSD analysis capability. A complete capability demonstration also requires all supporting pieces of a new workflow to be covered. Many of these supporting pieces are covered in an idealized manner. For example 3D geometry and meshing is a critical piece for such a capability yet dealt in a crude and coarse manner adequate only for the purposes of capability demonstration. The comparisons shown at the end between predictions and measurements are therefore not true validations but only a basis for qualitative verification. Nevertheless they provide the first glimpse of the kind of detailed stress/strain analysis possible using integrated 3D aeromechanics.

The paper is organized as follows. Following introduction, the paper begins by describing the new workflow. The next section describes the 3D CSD solver. The external CFD solver used for coupling is then briefly summarized. The fourth section describes the construction of 3D structural models. The fifth section covers the 3D CFD/CSD formulation — interfaces (spatial coupling) and the solution procedure (temporal coupling). The final section presents results from a fully integrated 3D analysis. The paper ends with some concluding observations.

INTEGRATED 3D WORKFLOW

Integrated 3D analysis requires a new workflow. The key pieces of this workflow are envisioned in Fig 1.

The workflow begins with a CAD model. It can be a gross description in the early stages of structural design, then progressively refined and populated with details as the design advances. The CAD geometry is then interpreted into a Structural Analysis Representation (SAR) geometry by the dynamicist. The SAR includes only those parts considered necessary for analysis and identifies them as a flexible part, a multibody part, or a device part. Flexible parts are marked for 3D meshing, multibody parts are assigned their functionality (joint type and constraints), and device parts are noted for special-purpose treatment. The flexible parts are those with significant strains. The multibody parts are idealizations of constraints that allow arbitrarily large relative motions between flexible parts. Devices are special-purpose parts which allow off-line character-

istics to be included (e.g. look-up tables for a non-linear lag damper). The next task is to mesh the flexible parts. Once meshed, all parts are re-integrated into a Structural Analysis Model (SAM) geometry. The SAM task merges all 3D parts, prescribes material properties, designates constrained nodes for multibody connection, defines the matematical properties of all joints (rotation order, locked versus free states and command signals), defines the physical properties of all joints (stiffness, damping, actuation force and ± free play), and completes the appropriate description of devices. The completed SAM is then ready for the CSD solver. All of these tasks fall under the broad category of 3D geometry and meshing (a companion paper [9] is devoted to this category).

A CSD solver must be equipped with special capabilities for rotorcraft — a pure structural dynamic analysis will not do. An internal aerodynamic module is needed for efficient coupling with CFD. A trim module is needed to achieve the mean rotor operating state. These require a top level description of aircraft geometry and configuration. Trim requires integrated loads (inertial and aerodynamic) at the hub from multiple load paths across multiple parts for which a specialized hub loads module is needed. A high-fidelity interface is needed for 3D fluid-structure coupling. The solution procedure for coupling is special and requires all of the above modules. All of these pieces are grouped within the broad category of a rotor dynamic solver. The 3D fluid-structure interface piece is generic to any external CFD solver (with structured or unstructured surface mesh). The CFD solver used in this work is part of the HPCMP CREATE™ – AV Helios software. This required the CSD solver to be incorporated within the Helios environment. This environment is presently equipped to execute a CSD solver from only a single processor — as per requirements of current generation comprehensive codes. While this is not a barrier for the main emphasis of this paper it prevents the Structural Partitioning piece of the workflow from implementation (Fig 1). It also prevents meaningful timing conclusions to be drawn.

3D ROTOR DYNAMIC SOLVER

The 3D rotor dynamic solver consists of a core 3D solid-multibody CSD solver, an aircraft geometry module, an internal aerodynamics module, a hub loads module, a trim module and a 3D fluid-structure interface module. The fluid-structure interface module is described in detail in a later section. The present work considers only an isolated rotor so the aircraft geometry module is not used. A brief summary of the rest are provided below.

3D Solid-multibody CSD Solver. The flexible parts of a structure are solved by 3D governing equations of motion derived in a rotating frame (non-rotating is a simplification) using generalized Hamilton's Principle. The formulation uses Green-Lagrange strains and second Piola-Kirchhoff stresses for strain energy and follows a geometrically exact nonlinear Total Lagrangian formulation. Exact geometry and strains are a pre-requisite for unifying multibody dynamics within 3D. The stress-strain relationship is linear. Isoparametric, second order, brick elements: 27-node hexahedral elements and 10-node tetrahedral elements are available for discretization of the structure. See Ref [2] for details.

The multibody connections and constraints use Euler angle joints. A special formulation is used which preserves kinematic exactness between 3D elements undergoing arbitrary rotations relative each other while at the same time eliminating all algebraic constraint equations. The special formulation is a joint that is associated with 12 states — 6 are interface states that constrain the position and orientation of the joint in space and another 6 are the joint states that describe its deformation. The joint states can be constrained (locked), commanded (prescribed) or actuated (forced). Connections are also special in 3D — they represent true connections. Connection points must be identified precisely on the flexible parts and a mesh generated with nodes available at those locations. If the connection points are not known a priori a generic connection can be used that constrains an entire face of the flexible part. The internal stresses at the edge will then be incorrect but the kinematic exactness will still be preserved. See Ref [3] for details.

Three classes of algebraic solvers are available: direct, iterative, and eigen. The direct solver is a skyline solver. The iterative solvers are iterative-substructuring solvers based on Finite Element Tearing and Interconnecting - Dual Primal preconditioners and equipped with Conjugate Gradient and Generalized Minimum Residual updates. The eigen solvers are not developed as part of this work but available as calls to external scaLapack routines [10]. The direct solver is most efficient on a single processor but not parallel. The iterative solvers are parallel and scalable and meant for large scale distributed execution. The eigen solvers are parallel but not scalable. Because the present environment restricts the solver to a single processor the direct solver is used.

The algebraic solvers are the building blocks of structural solvers. Two types of structural solvers are available, both employing a direct time integration of the second order nonlinear structural dynamic equations. The first is a single time-step Generalized-α Method [11] and the other is a two time-step trapezoidal plus three-point backward Euler combination [12]. The 3D solid-multibody models are strongly nonlinear and the dynamic stiffness matrix must be updated at every time step for accuracy of the response solution. Additionally, structural sub-iterations (Newton-Raphson) are possible within both classes of solvers, but required only for relatively large time steps.

Internal Aerodynamics. The internal aerodynamics model, presently, is only meant to support CFD coupling, hence elementary: quasi-steady linear aerodynamics with uniform inflow. Its purpose is to provide airload sensitivities to blade deformations (aerodynamic damping) so non-circulatory airloads are also required (for torsion damping). Aerodynamic angles (angle of attack α and sideslip β) are extracted from the 3D deformation field using the deformed chord orientation relative air flow and blade velocities at $3/4 - c$ location (see section on 3D Structural Models) as per thin airfoil theory. Both angles and rates are required for the angle of attack. There is no aerodynamic damping in lag so either a damper model is needed (a simple linear model is used here) or artificial damping added and bled out consistently to decay initial transients. Transients in lag dynamics make a direct integration in time to periodicity an expensive solution process. Even with the known damper value for this existing rotor about 15 revolutions are needed to decay any lag transients.

Hub Loads. The root shears and moments in the rotating frame are calculated either by force summation or from joint reactions. The counterpart of the deflection method in beams is a direct stress integration in 3D. Stress integration is available for the flexible parts but at the ends or at the joint connection points — where the integrated loading is actually desired — 3D edge effects or local concentration effects occur and contaminate the solution. The effects are real but require a high local mesh resolution to capture. The contamination of global trim solution with local mesh resolution is considered unacceptable. Thus force summation or joint reactions are needed instead of the stress integration method. (Note that even in beams shear forces cannot be resolved directly — if at all — using deformations and a force summation is always needed). These are needed also for elements that are idealized to be rigid. The force summation method is same in principle as in beams except that a volume integration is needed in 3D. For a converged response both should be identical (see section on 3D CFD/CSD Analysis Results) even though in general force summation is more accurate for higher frequencies and larger time steps. Joint reactions are needed for multiple load paths. Here joints are used as sensors which means they have to be assigned a small flexibility in the direction (and type) of the desired loading. Thus, strictly, sensing alters the dynamic characteristics of the model — but is not inconsistent with the real behavior of systems.

Trim Solution. Once hub loads are obtained the trim solution is straight forward. Presently only isolated rotor options are available: wind tunnel trim (targets are thrust or coning and two cyclic flapping angles), moment trim (targets are thrust or coning and two hub moments) and propulsive trim (targets are lift and propulsive force and either two cyclic flapping angles or two hub moments). The control inputs are via joint commands (additionally shaft tilt for propulsive trim) imposed either at the blade root bearing or at the base of the pitch link.

3D CFD SOLVER

The CFD solver used is part of the HPCMP CREATE™ – AV Helios software. It is an integrated capability consisting of an unstructured, node-centered, implicit RANS (Spalart-Allmaras turbulence) near-body solver, an overset Cartesian, explicit, Euler off-body solver, and an implicit hole-cutting based domain connectivity algorithm. The solver has been extensively validated with current state of the art beam models for the same rotor used in this paper. A description of its general architecture can be found in Ref [13]; validation of its aerodynamic and CFD/CSD capabilities can be found in Ref [14].

The aerodynamic set up is identical to Ref [14]. A coarse mesh set-up is used. The near-body grid contains 4.5 million points and extends up to 5.8 chords. The off-body grids contains about 14 million nodes (finest spacing of 0.18 chord) and extends up to 58 chords. An azimuthal discretization of 0.25° is used with 25 sub-iterations for the near-body solver and a single sub-step for the off-body solver. The Courant-Friedrichs-Lewy number for the off-body solver for this time step is 1.67. The CFD solver is executed on 128 processors.

3D STRUCTURAL MODELS

A four-bladed fully articulated rotor model is considered. Each blade is an assembly of several flexible and joint parts. The lag damper is not modeled as a separate device but included as a linear damper as part of a joint. Two different configurations (baseline and simple) and two different blade meshes (baseline and simple) are constructed for this study. The baseline configuration and the baseline blade constitute the full-up model. All results shown are from the full-up model unless otherwise mentioned.

The baseline configuration consists of four flexible parts, three joint parts and two load paths (see Figs 2 and 3). The flexible parts are the blade, the hub block, the pitch horn and the pitch link — all modeled using 3D elements. The blade contains 592 or 48 hexahedral elements (see later), the hub block 8, the pitch horn 3 and the pitch link 3. Joint 1 is a spherical joint located within the hub block and represents the elastomeric flap-lag-pitch bearing at the root end. It is connected to three flexible parts — the blade, the hub block and the pitch horn. It transfers blade loads to the hub block and pitch horn control motions to the blade. Joint 2 is another spherical joint located between the pitch horn and the pitch link. Joint 3 is a slider joint located at the bottom of the pitch link and represents the connection to the swashplate. It is free to roll and pitch relative to

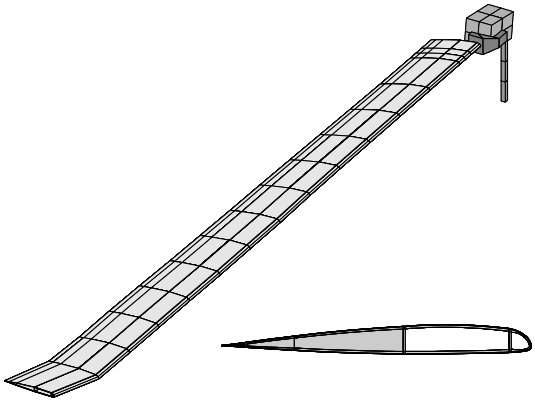

Figure 2: **3D model of an UH-60A -like rotor.**

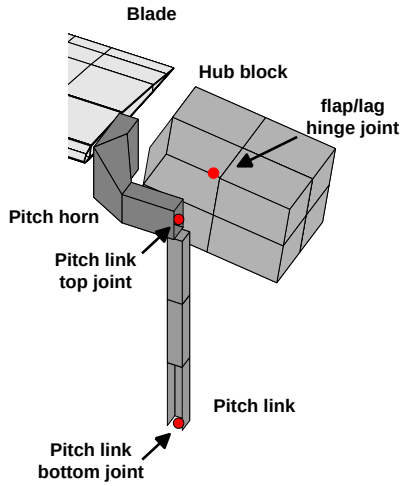

Figure 3: **Close-up of rotor hub.**

the swashplate but locked in yaw. The control angles are imposed as a linear motion command at this joint. A simpler configuration consists of only the blade, the hub block and joint 1 all on a single load path. The control angles are then imposed as an angular motion command at the joint. The position and orientation of the joints are based on the UH-60A configuration. The properties of joint 1 — the stiffness and damping of the elastomeric bearing — are from the Army/NASA master data base. The lag damper is assigned to this joint. The properties of joint 2 are unknown and left as zero. The pitch link stiffness is introduced either as a linear spring at the pitch link bottom joint (baseline configuration) or added to the pitch stiffness at the bearing (simple configuration). Note that the elasticity of the pitch link adds to the net control system stiffness in the baseline case. For this reason the blade root pitch angles under trim conditions differ marginally for the two configurations.

The baseline blade has an SC1095 profile (Fig 2) with a realistic internal structure. Each section (or segment in 3D) consists of 37 hexahedral elements with 27 nodes each (592 cross-sectional nodes in total) with 16 spanwise segments in all. The grid is coarse and constructed using a simple in-house grid generator. The cross-sectional grid is guided by Ref [15] but modified for second-order elements and then extruded in the spanwise direction accounting for quarter-chord axis, built-in twist, and tip sweep. A simpler blade has the same spanwise construction but a fake rectangular solid cross-section. The full-up model — baseline configuration and baseline blade — contains $17,566$ degrees of freedom.

The baseline blade requires a detailed description of material properties. The material properties are unavailable in the public domain so values are assigned such that they generate cross-sectional structural properties similar to the UH-60A. This requires a heterogeneous material assignment with different values for the box beam, skin, core, and leading edge elements. In general a 6×6 material matrix can be assigned to each element; here isotropic properties are considered within each element. The same profile and cross-section is used at all span stations, thus, the chord length and structural properties remain uniform. The assignment of material properties to generate the target set of cross-sectional properties is carried out iteratively. The cross-sectional properties can be estimated from static deflections to prescribed forcing using the 3D analysis itself — a process similar to that of static testing of blades.

For the extraction of sectional properties, and for the contruction of aerodynamic interfaces later, blade cross-sections must be defined. Figure 4 describes the definition (blade twist and some surface elements removed for illustration). Elements must supply nodes at the leading and trailing edges and these nodes have to be designated up-front as part of the model input. The analysis then defines the chord line and locates the $1/4-c$ (needed for CFD interface) and $3/4-c$ (needed for classical aerodynamics) points. Two additional nodes, one on the top surface and another at the bottom, are required to define a nominal thickness line. It is used to simply define the cross-sectional plane. It need not be perpendicular to the chord line thus any two points suffice as long as they are on the top and bottom surfaces. The key requirement is that all element faces line up along the section. Thus even though the solver is naturally unstructured, sections can only be defined at span stations where the elements line up. The geometry and grid must be described accordingly for all span stations where sectional analysis is needed.

If e_c is an unit vector aligned along the chord line

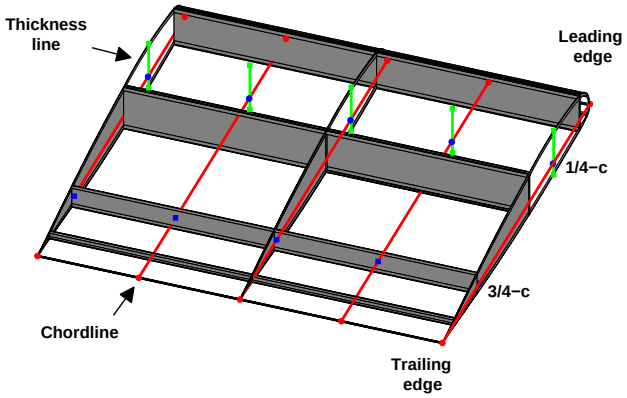

Figure 4: **Definition of cross-sectional planes.**

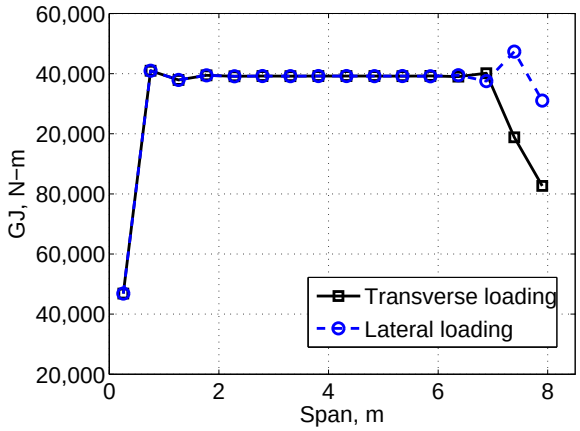

Figure 5: **Calculation of torsional rigidity GJ.**

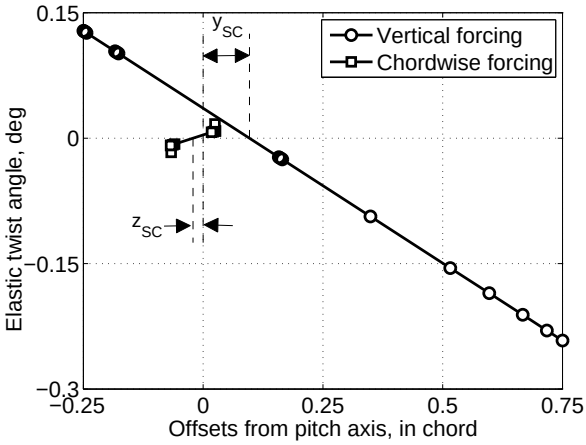

Figure 6: **Calculation of elastic axis.**

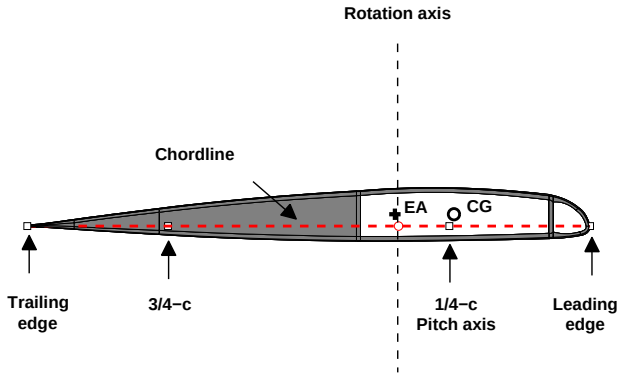

Figure 7: **Cross-section of the main blade.**

(trailing edge to leading edge) and t an unit vector along the thickness line (bottom surface to top surface) then the unit vectors along the axial and normal directions are defined as the cross products

$$\begin{aligned} e_a &= \widetilde{e_c}\, t \\ e_n &= \widetilde{e_a}\, e_c \end{aligned} \tag{1}$$

As the blade deforms the orientation of e_a, e_c, e_n can be used to extract a set of beam-like cross sectional rotations. Elastic deformations can be found by subtracting the baseline geometry consisting of the built-in twist (swept tip consists of sheared sections for this rotor). The deflection of the $1/4 - c$ point can be used as the cross-sectional linear deflection.

The sectional property calculation is performed as follows. Note that this step is not needed for 3D analysis but only used as a means for backing out the unknown 3D material properties. There is no unique inverse solution so an approximate representation is sought by trial and error. The inertial properties and flexural constants are obtained directly from geometry and material descriptions. The torsional stiffness GJ and the shear center require static solves. The steps are as follows:

1. Obtain sectional mass, center of gravity (C.G.), area and center of area (C.A.), and axial stiffness EA.
2. Obtain Principal Axes, bending stiffnesses flap and lag EI about C.A. along Principal Axes, moments of inertia about C.G. along Principal Axes, and C.G. and C.A. offsets from $1/4 - c$ along Principal Axes.
3. Introduce a pure couple at the blade tip; calculate spanwise twist gradient ϕ' and reaction torque τ by stress integration. Calculate $GJ = \tau/\phi'$.
4. Introduce a series of forcing at the tip in vertical and chordwise directions to identify the shear center.

Steps 1 and 2 are straight forward. For steps 3 and 4 an uniform blade is constructed (zero built-in twist and sweep) with the cross section. In step 3 a pure couple is introduced at the blade tip using two equal and opposite nodal forces along any direction. The value of GJ calculated at sections away from the ends remain uniform as

shown in Fig 5 and considered to be the cross-sectional value. The calculations deviate near the root due to edge effects and the tip due to proximity to applied forcing as expected. For the rectangular cross-section the classical St. Venant constant is recovered. The calculation of the shear center is show in Fig 6. Elastic twist from a set of vertical and chordwise forcing are interpolated to find the zero cross over point and identify the location of the shear center. For no bending-twist coupling the shear center is a cross sectional property and remains uniform with span.

The blade cross-section with the calculated offsets are shown in Fig 7. Note that the blade is placed with pitch axis ahead of the rotation axis by the torque offset. The C.G. is placed close to and ahead of the pitch axis at $1/4-c$. Then stability is guaranteed in the thin airfoil sense (aerodynamic center at $1/4-c$). But the E.A. falls significantly behind the C.G. (by 13% c) which results in a strong flap-torsion coupling. The effect of this coupling is seen later in airloads. The C.G. location relative pitch axis is similar to that of the UH-60A but its offset relative E.A. is a substantial deviation.

3D CFD/CSD FORMULATION

The 3D CFD/CSD formulation includes the interface (spatial coupling) and solution procedure (temporal coupling).

The interface deals with deformations sent to CFD and surface forcing sent to CSD. The deformations can be described in one of two ways: as a 2D beam-like field or as a 3D field. The surface forcing can be described in one of three ways: as 2D segmental airloads, as 3D patch forces, or as 3D surface pressures and shear. It is assumed that the discretized surface will always differ between CFD and CSD and hence corrections will be required for conservation (same virtual work) and consistency (same integrated forcing). The difference is not merely from mesh mis-match but unavoidable geometry mis-match — aerodynamic design will define the surface first while structural design will populate the surface last. Thus a method is desired that can be applied even when the internal structure is at an early design stage and does not necessarily carry on to the wetted surface.

Deformation Interface

A 2D beam-like description of the deformation field allows the airfoil shapes in the fluid domain to be kept intact. While this description is the natural state of the art in beams, in 3D, they must be extracted from the deflection field. The extraction is based on the deformed chord and thickness lines that describe the deformed orientation of the cross sectional plane. The cross sectional planes are defined as shown earlier in Fig 4. The extraction excludes any cross-sectional flexibility — beyond what is captured by the four nodes that define the lines — and appears to defeat the purpose of a 3D interface but is indeed the only means by which structures that are internally incomplete can be analyzed. Thus integrated 3D stress/strains can still be obtained at early stages of structural design when only the main load-bearing pieces may be in place. The extraction procedure is straight-forward: the direction cosines of the deformed cross-section: e_a, e_n, e_c, are used to extract three Euler angles for any order of rotation. Standard limitations near $\pm\pi/2$ apply but seldom encountered in rotor problems. The order used here is lead-lag, flap, and pitch, consistent with mesh deformation.

A 3D description of the deformation field encounters the problem of geometry and mesh mis-match. Ideally, there is a common 3D CAD geometry that populates both sides of the interface — CFD and CSD — so that a point in either domain can be associated with a corresponding point on the other via geometry. A common geometry description is beyond state of the art so the CFD mesh is presently considered to be the exact geometry. The problem then reduces to associating each CFD mesh point with its counterpart on the CSD surface. This parameterization is different in 3D and is the basis for constructing an exact interface. Here exactness is defined as errors introduced due to interface mis-match not exceeding those that are introduced by the discretization of the individual solvers themselves. The parameterization is described under Level-II Force Interface later.

Level-I Force Interface

The level-I force interface is an extension of the lower order aerodynamic interface with 2D airloads admitted from CFD. Guaranteeing conservation is not possible but consistency is achieved by the use of segmental airloads (integrated over span-wise segments, see Refs [14, 17] for methodology and validation). These airloads must now be distributed over the surface nodes of the segmental 3D elements. The nature of 2D airloads implies the 3D finite element grid must ensure sets of surface elements along spanwise strips. Elements can be unstructured within the strip but set boundaries must line up along the chordwise direction. Then all surface nodes within a segment are identified as aerodynamic interface nodes.

In the present mesh the 3D elements are naturally aligned in the spanwise direction therefore segments are easy to define. Figure 8 shows two spanwise element rows (blade twist and some surface elements removed for illustration). Because the elements carry internal nodes there are five spanwise nodal lines. Assume the two ends represent the root and the tip. Then the aerodynamic segments span half-way across either side of each nodal line. So there are as many segments as there are nodal lines. Each segment receives dimensional air-

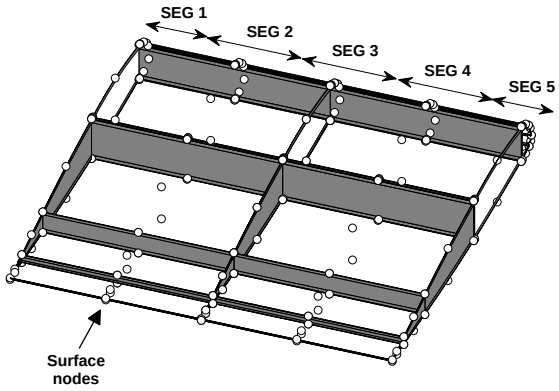

Figure 8: **Level-I force interface.**

loads from CFD with pitching moment about the $1/4-c$. These are then distributed over the segmental nodes in an assumed manner — linearly for lift (along chord, increasing toward leading edge) and quadratically for drag (along thickness) — as functions of three constants to be solved at each azimuth and radial station from the CFD airloads. If y and z are the chordwise (toward leading edge) and thickness wise (to upper surface) coordinates and F_Z, F_Y and M are the vertical, in-plane and $1/4-c$ pitching moments then the nodal forces f_Z and f_Y in the vertical and in-plane directions are represented as

$$\begin{aligned} f_Z &= \alpha_0 + \alpha_1(y - y_{25}) \\ f_Y &= \beta_0 + \alpha_1(z - z_{25})^2 \end{aligned} \tag{2}$$

with the three constants α_0, α_1 and β_0 solved using the three airloads

$$\begin{aligned} F_Z &= \sum f_Z \\ F_Y &= \sum f_Y \\ M_{25} &= \sum \left[f_Z(y - y_{25}) - f_Y(z - z_{25}) \right] \end{aligned} \tag{3}$$

The subscript 25 denotes $1/4 - c$ quantities. The summation is over all n segmental nodes. The axial force F_X, although negligible compared to the inertial force, is simply distributed at each node as $f_X = F_X/n$.

The internal stresses from the level-I interface are only as good as the assumed representation and therefore ad hoc. It is a convenient interface for initial verification because it leaves the Delta Coupling procedure intact. This interface is used later for a fully coupled solution. But a 3D CSD model opens opportunity for a detailed interface with which exact internal stresses can be calculated. This is described below.

Level-II Force Interface

The level-II force interface is an exact 3D patch force interface. Consistency is guaranteed but conservation achieved only at the limit of fluid and structural mesh refinements. In this interface each CFD surface mesh point (or the center of each surface triad or quad — depending on how the surface stresses are integrated in the fluid domain to generate a patch force) is first associated uniquely with a CSD surface coordinate. Ideally, as noted earlier, a point on the exact geometry should be associated not a point on the CFD mesh, but in absence of a geometry module that populates both sides of the interface, the CFD mesh is assumed to be the exact geometry. The method is generic to mis-matched meshes. Given a CFD surface point — regardless of whether it lies on the CSD surface or not — an unique set of CSD surface parameters are calculated. This parameterization is based only on the natural coordinates and shape functions of the elements.

Within an element (including its surface) the geometric coordinates are related to the curvilinear natural coordinates as

$$\begin{aligned} x &= x(\xi, \eta, \zeta) \\ y &= y(\xi, \eta, \zeta) \\ z &= z(\xi, \eta, \zeta) \end{aligned} \tag{4}$$

where $-1 \le \xi, \eta, \zeta \le 1$. Because the relationship is nonlinear, given a target point $(x\ , y\ , z)_T$, its corresponding natural coordinates $(\xi\ \eta\ \zeta)$ must be found iteratively. The iterations can be started from any of the element nodes — where both $(\xi\ \eta\ \zeta)_0$ and $(x\ y\ z)_0$ are known — and continued as per Newton-Raphson to convergence.

$$k = 0, 1, 2, \ldots$$

$$\begin{bmatrix} x_\xi & x_\eta & x_\zeta \\ y_\xi & y_\eta & y_\zeta \\ z_\xi & z_\eta & z_\zeta \end{bmatrix} \begin{pmatrix} \Delta\xi \\ \Delta\eta \\ \Delta\zeta \end{pmatrix}_k = \begin{pmatrix} x \\ y \\ z \end{pmatrix}_T - \begin{pmatrix} x \\ y \\ z \end{pmatrix}_k \tag{5}$$

The left hand side gradient matrix (where $x_\zeta = \partial x/\partial\xi$ and so on) is the transpose of the Jacobian of the coordinate transformation. As long as the target point lies within or on the element and the element is well-behaved (i.e. has a well-conditioned Jacobian) the iterations will converge to an unique solution. Thus if the CFD point is on the surface (matched interface) its natural coordinates can be readily obtained using this basic procedure. A generic procedure is one that will obtain a corresponding set of natural coordinates for all points including those that are out of surface but collapse to the basic procedure for points on surface. Two different generic procedures are proposed as follows.

Method 1: Gradient extrapolation. Let $\zeta = 1$ be the surface (see Fig 9). An out of surface point is associated with a surface point (ξ, η) if the surface coordinate ζ leaves the surface in such a direction that it passes through the point. Thus the method can be termed a gradient extrapolation method as the gradient of the surface coordinate (ζ) is extrapolated. Note that all out of surface points that lie along the direction of extrapolation will be associated with the same — but unique

— CSD point. To identify this point the same iterations as Eq 5 are used but the gradient matrix is always evaluated at the surface ($\zeta = 1$ in this example). The iterations will drive the absolute value of ζ to greater than 1, confirming the point lies outside the surface, but will converge in ξ and η. If not, or if the absolute values of either of these converged coordinates are greater than 1, then the point is rejected by the $\zeta = 1$ surface. All surfaces defined as fluid interfaces are checked one by one and if the point is rejected by all it is rejected by the element. If rejected by all elements it is eliminated from the interface and tagged instead as a candidate for error calculation. Figure 9 shows an example of successful extraction of surface parameters using this method.

Method 2: Orthogonal projection. Let $\zeta = 1$ be the surface (see Fig 9). An out of surface point is associated with the nearest surface coordinate (ξ, η) (note that this is not the nearest neighbor method where the association is to the nearest node). This means the normal to the surface at that coordinate passes through the point. The surface coordinates are obtained by

$$k = 0, 1, 2, \ldots$$

$$\begin{bmatrix} x_\xi & x_\eta \\ y_\xi & y_\eta \\ z_\xi & z_\eta \end{bmatrix} \begin{pmatrix} \Delta\xi \\ \Delta\eta \end{pmatrix}_k = \begin{pmatrix} x \\ y \\ z \end{pmatrix}_T - \begin{pmatrix} x \\ y \\ z \end{pmatrix}_k \tag{6}$$

A Moore-Penrose inverse of the left hand side matrix ($A^+ = (A^T A)^{-1} A^T$) solves the above equation in the least square sense and finds the nearest surface coordinate. If the absolute values of either of the converged coordinates are greater than 1 then the point does not belong to the $\zeta = 1$ surface. As in method 1 all surfaces of all elements are checked one by one for inclusion or elimination from the interface. Figure 9 shows an example of successful extraction of surface parameters using this method. Figure 10 shows an example of rejection where the extracted surface parameters lie outside the element.

The surface coordinates produced by the two methods are different (Fig. 9). In general the farther the point from the surface the greater the difference. Only when the element boundaries are orthogonal the two methods converge. Because then the coordinate leaving the surface (used in method 1) is the surface normal (used in method 2). In general either method can be used with the difference compensated for by the interface error calculation (see below). For each CFD surface node the corresponding CSD element and its natural coordinates ξ, η, ζ then complete the surface parameterization. The displacement of each CFD node and the virtual work contribution of the patch force occurring at that node are now precisely defined.

Force interface error. Even though the interface is exact — the errors now stem entirely from geometry description of the individual solvers and not how variables

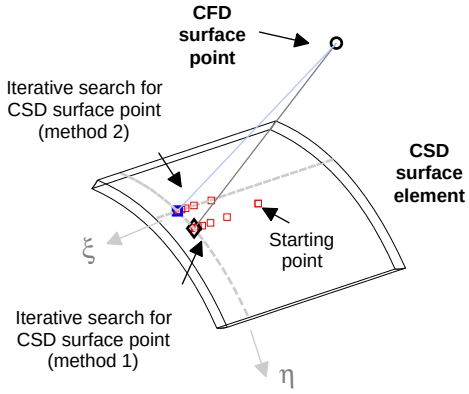

Figure 9: **An example of an out of surface CFD point for which CSD surface parameters could be extracted successfully.**

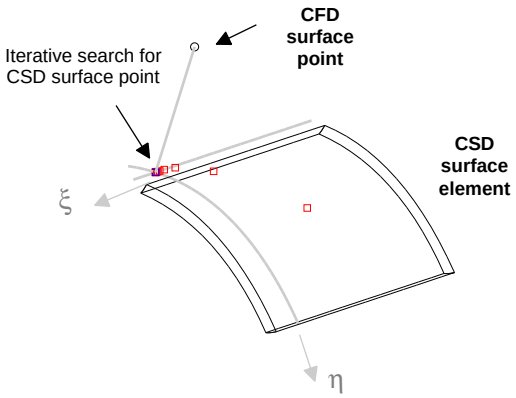

Figure 10: **An example of an out of surface CFD point for which CSD surface parameters could not be extracted successfully.**

are exchanged between them — it can lead to significant errors or can even break down (large number of points eliminated from interface) when the underlying structural model is incomplete. It is important that these errors be accounted for so that meaningful stress calculations are still possible at early stages of structural design. For this purpose the error is defined in terms of segmental airloads. For all CFD nodes that are eliminated from the interface (i.e., not claimed by any CSD element) the error is simply its contribution to the segmental airload. For all others, the error is only in form of a segmental pitching moment, calculated based on the distance between the CFD coordinate and its corresponding CSD coordinate. The segmental airloads (errors) are then reintroduced into the structure through a level-I interface. For no mis-match the error vanishes. For a 100% mismatch level-II collapses to level-I — since every point is then rejected and re-introduced through level-I.

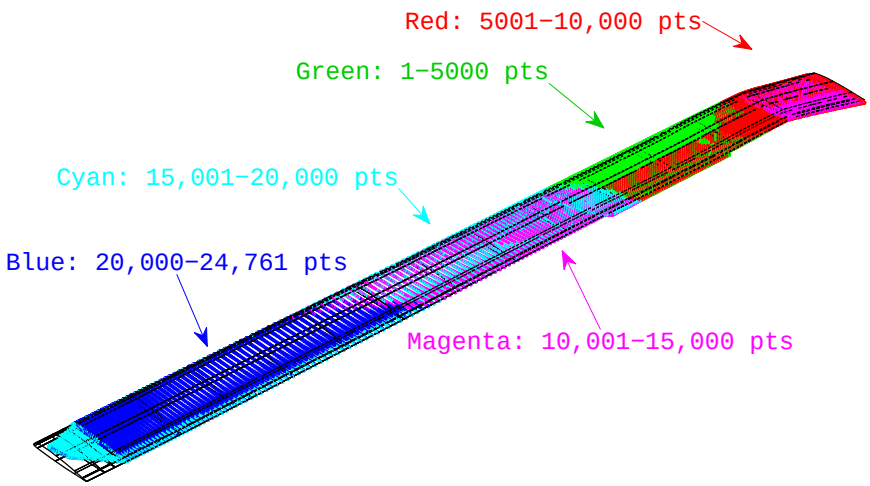

Figure 11: **CFD and CSD surface meshes for an UH-60A rotor.**

UH-60A example. The UH-60A near body CFD mesh is superposed on the UH-60A-like CSD surface elements in Fig 11. As expected there are significant mismatches in geometry and meshing. The surface parameters are now extracted using the two methods described earlier. Because the structural model has a coarse surface mesh a simple search algorithm suffices — each point is searched over all surface elements until claimed. The search process requires an additional check. For example if $\zeta = 1$ is the assigned surface then a CFD point is parameterized for both surfaces $\zeta = \pm 1$ and is admitted only if it is closer to the assigned surface. This prevents a CSD lower surface element claiming a point from the CFD upper surface. Pathological cases are still possible however for dramatic mis-match. For example if the CFD mesh is entirely below the CSD mesh then all points are claimed by elements at the lower surface and none by elements at the top. A common geometry description is needed to prevent such pathological cases.

Figures 12 and 13 show the eliminated points from methods 1 and 2 respectively. Most of these eliminations are easily explained — the structural model has no tab and there is a discrepancy in chord length on the swept tip portion — but method 2 eliminates a significant number of points near the leading edge. One such point is examined closely in Figs 14 and 15. Figure 14 shows that the point is eliminated because none of the elements provide a surface normal that passes through that point. The reason is that 3D elements are only C^0 (only displacements are continuous not slopes) thus there is a discontinuity in surface normals between elements. Points that lie in that gap are hidden from the interface. This is avoided by the gradient extrapolation method as shown in Figure 15. The gradient of the out of surface coordinate is always continuous across elements as long as they share a common face. Thus if the structural mesh ensures surface elements with common faces then the gradient extrapolation method appears to be the preferred method.

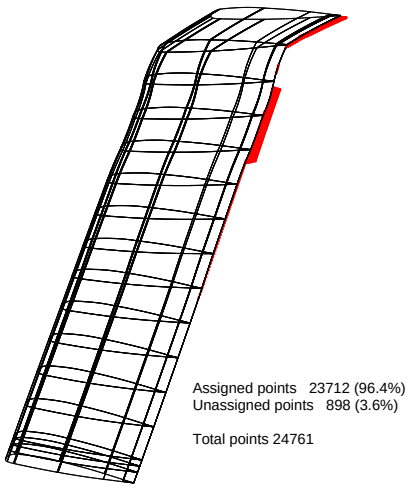

Figure 12: **CFD surface points (in red) eliminated from interface by the gradient extrapolation method (method 1).**

Level-III Force Interface

The level-III interface is a 3D surface pressure and shear force interface. The expression for virtual work

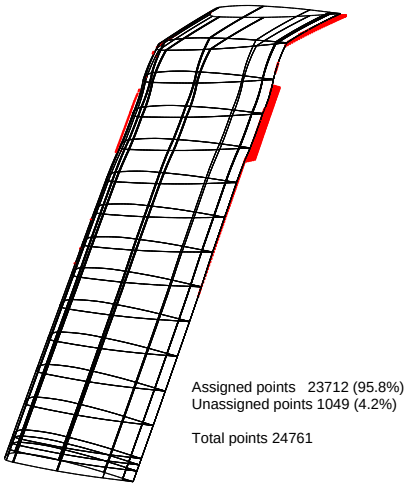

Figure 13: **CFD surface points (in red) eliminated from interface by the orthogonal projection method (method 2).**

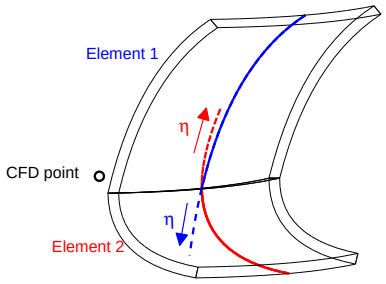

Figure 14: **A leading edge CFD surface point eliminated by the orthogonal projection method.**

integrates terms involving both fluid stresses and structural surface normals. Because conservation requires all interpolation to be carried out using corresponding shape functions in each domain [16], either fluid stresses must be supplied at all structural Gauss points (if integrating in the CSD domain) or structural shape functions supplied at fluid mesh points (if integrating in the CFD domain). Then conservation is guaranteed but consistency is still achieved only at the limit of fluid and structural mesh refinement. For different mesh resolutions the integrated forces will remain different in CFD and CSD domains. This is undesirable for rotor problems where accuracy of the trim state is essential. Thus the level-II interface is considered the most desired. The level-I interface is an approximation of level-II and is used for integrated analysis as the first step.

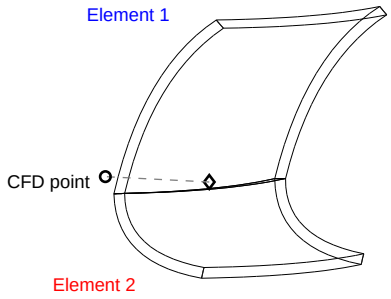

Figure 15: **A leading edge CFD surface point admitted by the gradient extrapolation method.**

CFD/CSD solution procedure

The level-I force interface is used. Thus the conventional Delta Coupling procedure of Johnson (Loose Coupling in rotorcraft terminology) can be retained with segmental airloads (dimensional) used as the delta variables. (Ref [18] is the original invention, the current implementation follows Ref [19]). The level-II force interface requires an advanced formulation with the surface element generalized loading used as the delta variables. This method was proposed and validated in Ref [17] for beams but not yet implemented in the current solver. The 2D deformation interface is used. Thus the conventional beam-like mesh deformation procedures can be retained in the CFD solver. The 3D deformation interface requires a mesh deformation method that is beyond scope of the current solver. Thus an integrated solution is obtained using the simplest of the interfaces.

As per the Delta Coupling procedure periodic airloads and deformations are exchanged. This accommodates unequal time steps in the fluid and structural domains naturally — 0.25° and 3° respectively — with airloads and deformations digitally filtered (Fourier interpolation, 12 harmonics used here) during exchange. Although airloads are available at the CSD time steps, deformations are not available at the CFD time steps, hence an interpolation is always needed. But because the CSD solution is obtained by time integration this interpolation cannot be made consistent with the solver while at the same time provide smooth grid motion across CFD time steps. Thus time accuracy cannot be ensured — not even at 3° intervals. The alternative — to march CFD and CSD together with intermittent sub-iterations — though straight forward is practically unacceptable in rotorcraft as the structural dynamics takes $30-40$ revolutions to attain the trimmed periodic solution whereas

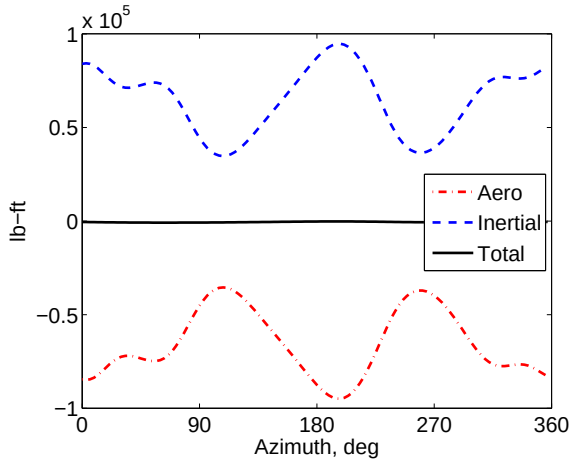

Figure 16: **Flap moment at root bearing.**

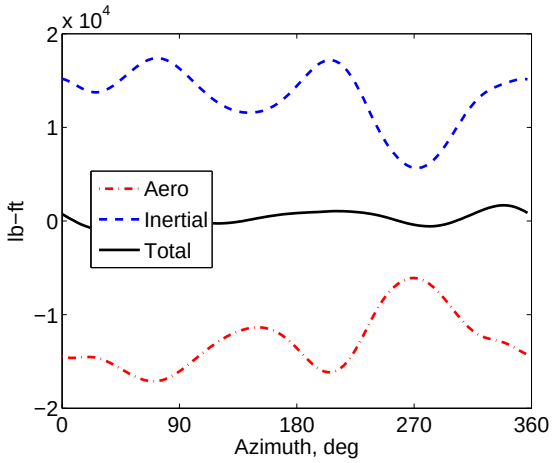

Figure 17: **Lead-lag moment at root bearing.**

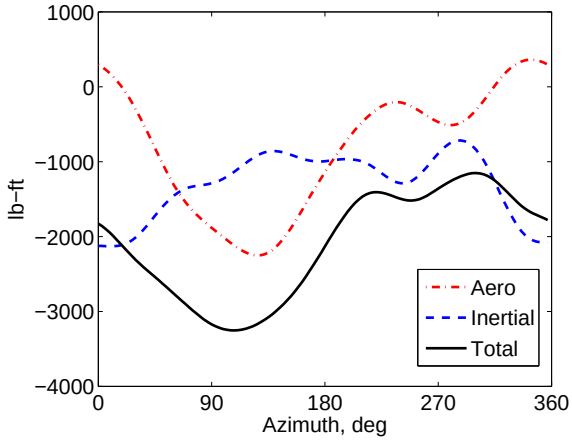

Figure 18: **Pitch moment at root bearing.**

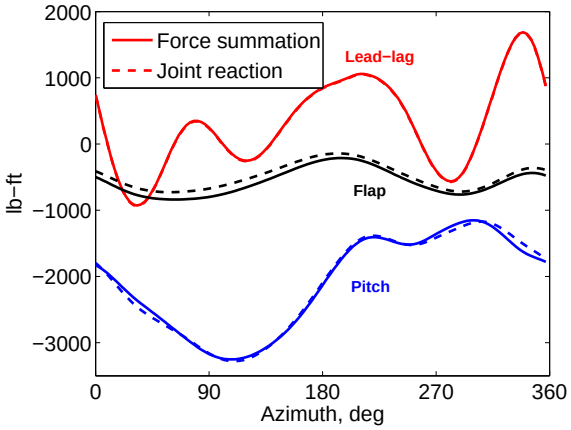

Figure 19: **Joint reactions at root bearing.**

the fluid solution settles rapidly to periodicity within $1-2$ revolutions. And because the fluid solution settles rapidly, advancing the solver by only a quarter of a revolution can allow nominally periodic airloads to be constructed using all four blades. The coupling process uses half a revolution for the first two CFD iterations and quarter revolutions there after.

As per the Delta Coupling procedure the simple internal aerodynamic model is retained in CSD as a preconditioner for convergence. An isolated rotor trim model is used with thrust and two hub moments targeted using collective and cyclic commands imposed as pitch link displacements. The trim Jacobian is calculated once using the internal aerodynamic model and requires no update for all coupling iterations for the flight condition studied.

3D CFD/CSD ANALYSIS RESULTS

The UH-60A flight test counter 8534 (advance ratio $\mu = 0.368$, nondimensional thrust $C_T/\sigma = 0.084$ and shaft tilt $\alpha_S = -7.31°$ (forward)) is considered. It is a high speed (158 kts) high vibration level flight where the dominant airloads are the 3D unsteady tip transonic pitching moments and hence CFD is essential. Even though the blade structural properties are not identical to UH-60A the aerodynamic characteristics (geometry and grid) are the same and therefore comparing predictions with UH-60A test data provides a reasonable basis for qualitative validation.

Dynamic Response

The time step required for stability and convergence of the dynamic response is observed to be governed by the nonlinearities introduced by the joint not the size of the finite element mesh. Thus the simple blade and the baseline blade both require the same time step for the same hub configuration. It is also observed that the dominant source of nonlinearity is the elastomeric bearing where the trim commands are imposed. Hence the simple hub and the baseline hub also have the same time step requirement — as the bearing is common to both. The strong nonlinearities require the calculation of dynamic stiffness at every time step. Calculating it once about a trim solution or updating it every few time steps

diverges the solution quickly. Under these considerations both time integration methods (the Generalized-α was executed at its simplest Newmark form) converges to the same results. Sub-iterations are possible at every time step but needed only for relatively large steps. Typically $3-5$ sub-iterations were required to drive the residual down to 10^{-5} at each time step. Sub-iterations are also required for the consistency of inertial loads with the response solution. For the purposes of CFD coupling smaller time steps were preferred over larger steps with sub-iterations so as to minimize errors from deformation interpolation. Thus instead of $\Delta\psi = 9°$ with $3-4$ sub-iterations, $\Delta\psi = 3°$ with no sub-iterations was preferred. The results shown are all obtained using $\Delta\psi = 3°$ with no sub-iterations.

The blade dynamic response is verified by studying the inertial loads and joint reactions. Simple aerodynamics (without CFD) is adequate for this purpose. To verify root reactions the simpler configuration is used where the pitch link stiffness is lumped at the bearing and the control angles are imposed as command signals at the bearing. Figures 16, 17 and 18 show the integrated aerodynamic, inertial and total (aerodynamic plus inertial) moments at the elastomeric bearing for flap (positive down), lead-lag (positive forward) and pitch (nose up) motions. The equal and opposite nature of the aerodynamic and inertial flap moments verifies the fundamental dynamics of the blade. It is not identically zero because of a small amount of stiffness and damping at the bearing. The damping is significantly larger in lag (due to the lag damper) which is reflected in the more substantial lead lag moment. The stiffness is significantly larger in pitch (due to pitch link stiffness) so that the root reaction follows the aerodynamic forcing closely. The inertial loading calculation, and hence the velocity and acceleration calculations, are verified by comparing these integrated moments obtained by force summation with reaction forces obtained directly from joint response at the bearing. This comparison is affected by the solver time step as mentioned earlier but agrees closely for $\Delta\psi = 3°$ as shown in Fig 19. The joint reactions are left in the joint frame to illustrate the effect of order of rotations. The force summation results are along the undeformed blade frame. Because the order of joint rotation is lead-lag first then flap and then torsion only the lead-lag comparison is exact, the flap and torsion moments have to be transferred to the undeformed frame for exact verification. Henceforth all results shown use the force summation method.

CFD/CSD Airloads

The convergence of the CFD/CSD analysis proceeds as shown by the mean normal force distribution from CFD in Fig 20. Iteration-0 shows CFD airloads calculated using deformations from the baseline trim solution (with internal aerodynamics). By Iteration-7 the airloads and dynamic response have nearly converged. Henceforth all airloads are shown from both the last two iterations 6 and 7. It is known that the flight test normal force shows a greater thrust at this condition than what can be achieved by the trim target.

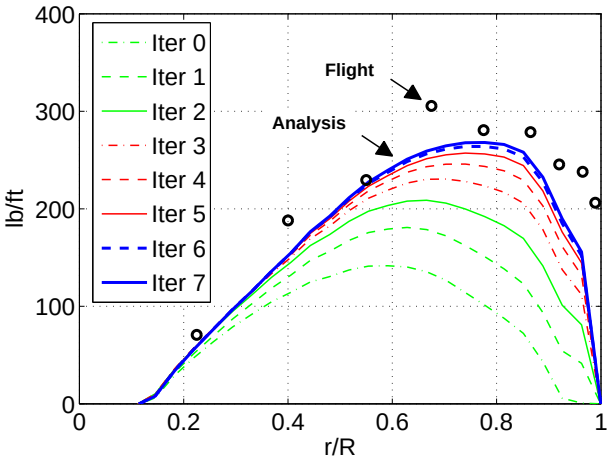

Figure 20: **Steady normal force convergence from 3D CFD/CSD using level-1 interface; predictions compared with measured UH-60A airloads for qualitative comparison.**

The detailed sectional airloads at three span wise stations are shown in Fig 21. Clearly the normal forces deviate significantly from the UH-60A values particularly at the outboard stations (inboard of 67.5%R predictions are good and hence not shown). The discrepancy is partly because of the less severe transonic pitching moment drop at the first quadrant close to the tip (96.5%R) due to a different blade dynamics than the UH-60A but mainly for reasons revealed in Fig 22. Figure 22 shows the harmonics of the normal force across the blade span. Forcing that are passed to CSD is plotted (divided by segment lengths) so the spanwise resolution is the same as the number of aerodynamic segments in the model (33 segments). The 1/rev phase with its distinct 180° shift over the span verifies the accuracy of the trim solution. All the vibratory harmonics ($3-5$/rev) are well predicted with at least the same accuracy achieved by current UH-60A beam models coupled to CFD. The main discrepancy is from the 2/rev airloads. These are determined by a large 1/rev torsion at this high speed condition. The 1/rev torsion in the current analysis deviate significantly from the UH-60A due to the very high (13% c) C.G. offset from the E.A. (Fig 7). The 1/rev torsion magnitude is as expected (about negative 4° peak to peak) but the phase is contaminated by 1/rev flap. Thus a proper validation of a 3D analysis requires a more careful assignment of material properties so that at least the major offsets (E.A. and C.G.) are precisely placed.

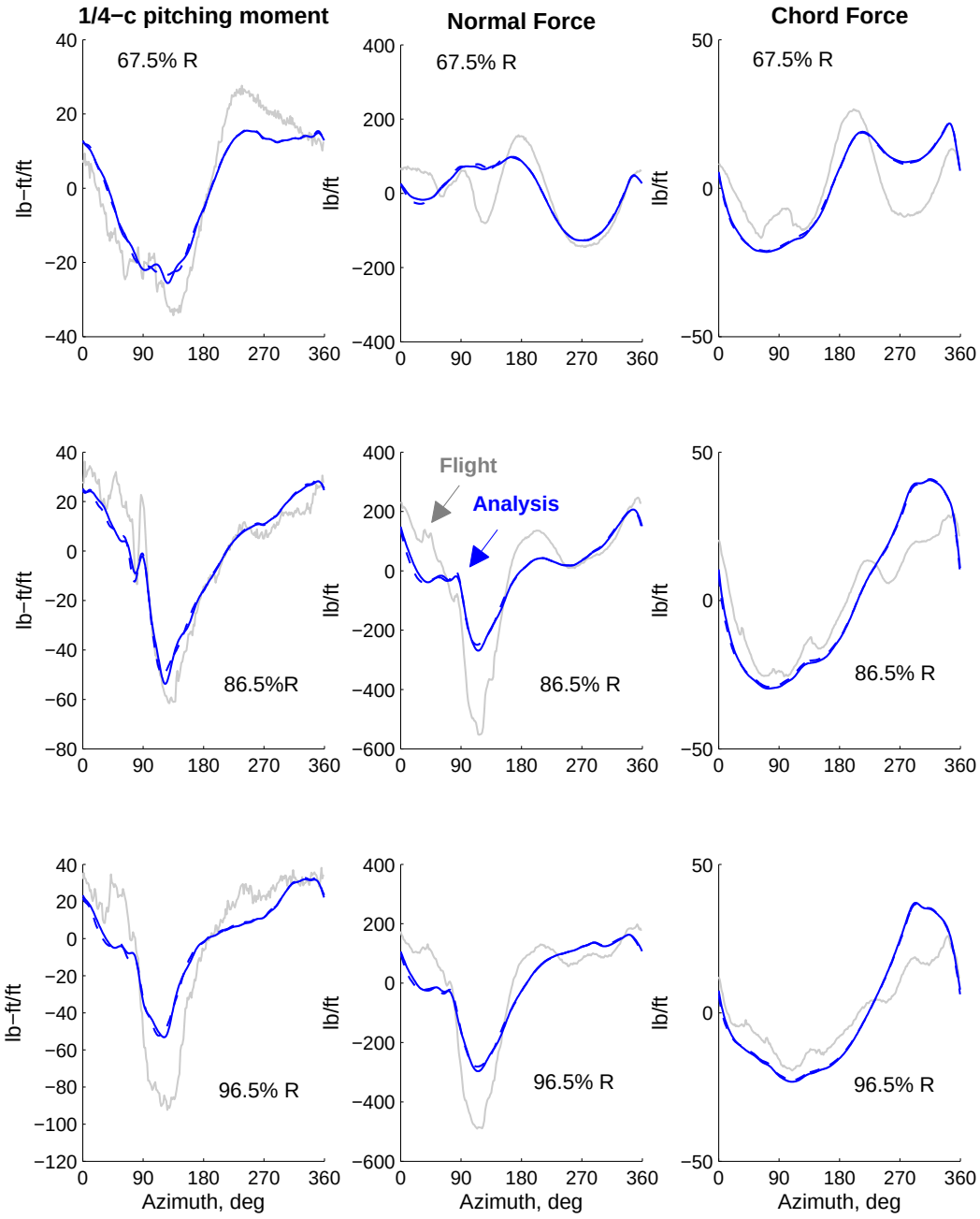

Figure 21: **Airloads from 3D CFD/CSD using level-1 interface; predictions from last two iterations compared with measured UH-60A airloads for qualitative comparison.**

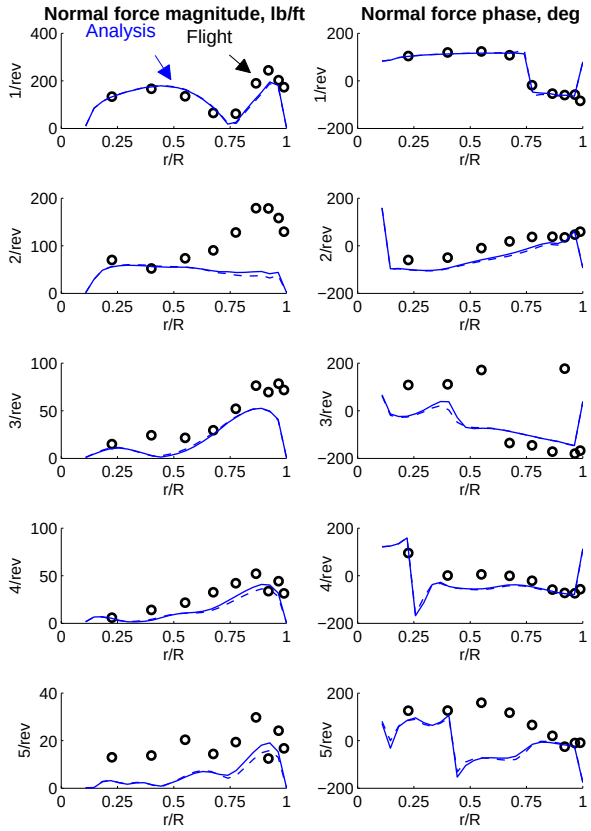

Figure 22: **Normal force harmonics from 3D CFD/CSD using level-1 interface; predictions compared with UH-60A airloads for qualitative comparison; symbols are flight test measurements, lines are predictions from last two iterations.**

CFD/CSD Dynamic Stresses

A 3D analysis enables the direct calculation of dynamic stresses and strains on all 3D flexible parts. Results from the blade are shown here. There is no data readily available for validation but because blade loads (bending moments) are measured by calibrating surface strains, validation is possible in principle.

The predicted tensile stresses (Cauchy stresses τ_{11} where 1 is nominally the radially outward direction) occurring at 77% R are shown in Fig 23 for every 45° azimuth. The airfoil section (expanded in scale) is overlayed for reference. The mean stress level is set by the centrifugal loading; oscillatory stresses arise from bending. As expected it is the main spar — the box beam at the center — that has the maximum loading and encounters the maximum variation. At 90° azimuth the maximum stresses occur at the flange-like top portion of the spar whereas at 270° they occur at the bottom. In general the top portion is loaded more heavily on the advancing side and the bottom portion on the retreating side. The loading at 0° and 225° are similar on the top and bottom implying that the bending curvatures are possibly close to zero at these azimuths. The web-like vertical portions of the spar do not show any significant oscillatory loading.

The loading pattern is studied in greater detail at eight locations on the cross-section (Fig 24) — two on the trailing-edge (one each near the top and bottom surfaces), four inside the spar (one on each arm) and two near the leading-edge (on each near the top and bottom surfaces). Figure 24(a) shows these sensor locations. Instead of stresses micro-strains (μ) are plotted versus azimuth (Figs 24(b)- 24(d)) since maximum safety of flight limits are often characterized by strains. These reflect not only the nature of the loading but also indicate the extent of cross-sectional flexibility. The strains are significant all over the cross-section. At the trailing-edge (Fig 24(b)) — where the sensors are close together — the strains are similar on the top and bottom surfaces as expected. But on the spar they exhibit a pattern similar to flap bending moments (Fig 24(c)). The typical rise in flap bending moment in the third quadrant is reflected as a reduction in strain on the top (increasing compression) and an increase in strain at the bottom (increasing tension). The pattern is almost symmetric except for an additional effect from chordwise bending. The peak-to-peak oscillatory strains are around 800μ on the top and bottom portions of the spar. The web-like portions on the back and front encounter relatively benign strains. The strains here reflect the chord wise bending moments. The chord wise stiffness is significantly higher than the flap wise stiffness and this is reflected in the lower strains. The strains at the leading-edge (Fig 24(d)) also exhibit similar characteristics as flap bending but the location of the top sensor is such that its behavior is closer to that of the front web sensor rather than the top surface.

The transverse shear stresses in the vertical direction (Cauchy stresses τ_{13} where 1 and 3 are nominally toward the tip and the top surface respectively) are shown in Fig 25. In general the shear stresses are an order of magnitude lower than the tensile stresses. Unlike tensile stress here the web-like vertical portions carry the maximum loading. Between 45°–180° the front web is more heavily loaded whereas from 180°–45° the loading is transferred to the back. But in general the rear web is loaded more heavily reflecting the generally nose down characteristics of the torsion loading — except in between 90°–135° where it possibly reflects the local wake induced loading in the advancing side. The rear web has generally greater stress levels than the front web perhaps affected by the relative positions of shear center and aerodynamic center. The transverse shear stresses in the in-plane direction (Cauchy stresses τ_{12} where 2 is nominally toward the leading-edge) are shown in Fig 26. These are similar in magnitude to those in the vertical

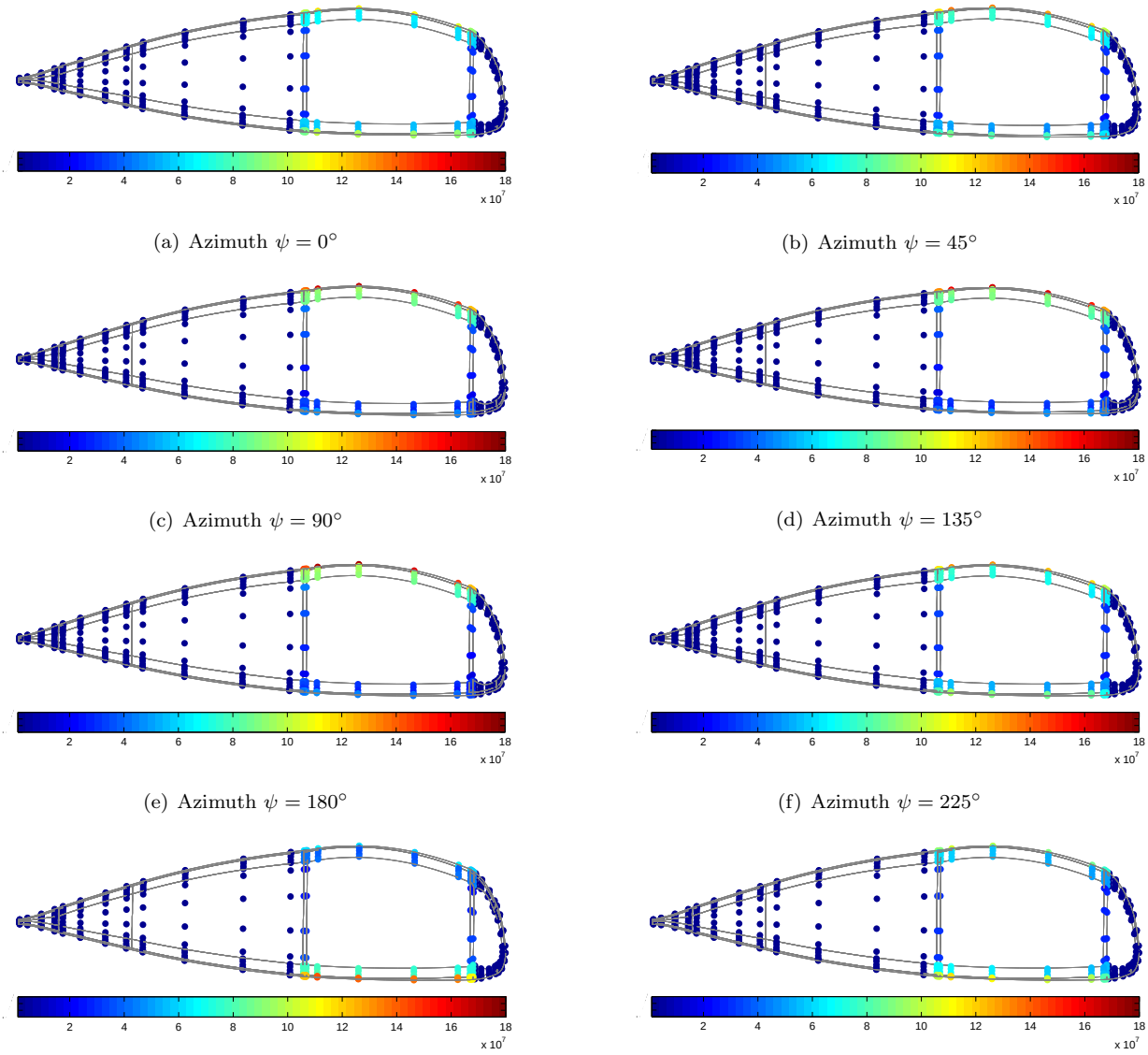

(a) Azimuth $\psi = 0°$

(b) Azimuth $\psi = 45°$

(c) Azimuth $\psi = 90°$

(d) Azimuth $\psi = 135°$

(e) Azimuth $\psi = 180°$

(f) Azimuth $\psi = 225°$

(g) Azimuth $\psi = 270°$

(h) Azimuth $\psi = 315°$

Figure 23: **Dynamic tensile stresses (τ_{11}) predicted using 3D CFD/CSD analysis; 77% R station; colormap range: $10^6 - 18 \times 10^7$ N/m^2 (Pascal).**

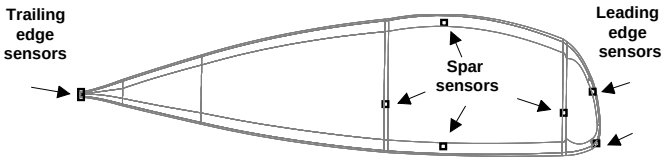

(a) Strain sensor locations; two at the trailing-edge, four on the main spar and two near the leading-edge.

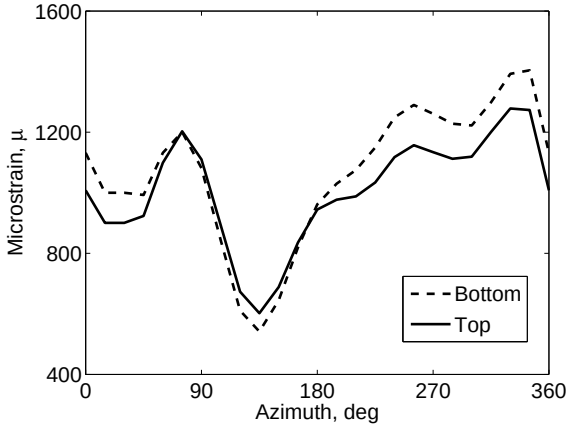

(b) Strains at the trailing-edge.

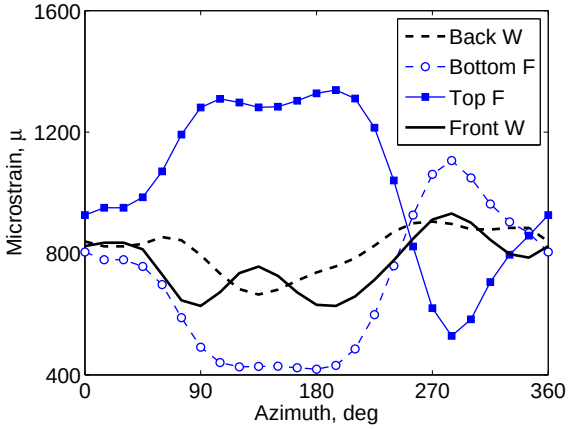

(c) Strains at the spar

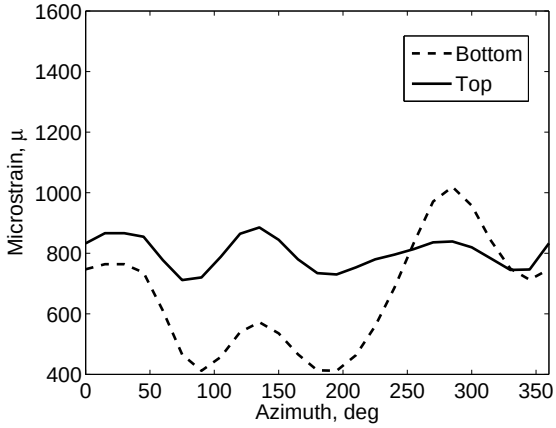

(d) Strains at the leading-edge

Figure 24: **Azimuthal variation of tensile strains (ϵ_{11}) predicted using 3D CFD/CSD analysis; 77% R station.**

direction but they occur at different locations. Like the tensile stresses, here the flange-like portions of the spar exhibit the maximum loading. But in terms of gross loading they exhibit the same general pattern as the vertical shears — the rear web is loaded more heavily reflecting the generally nose down characteristics of the torsion loading except in between 90°–135° azimuths.

The generic nature of the blade and the approximate nature of the level-I interface make specific conclusions on the details of stress/strain variations premature for this rotor but the results above appear consistent with typical patterns of loading and reveal the type of detailed stress/strain analysis possible using 3D structures.

CONCLUSIONS

A full three-dimensional finite element-multibody structural dynamics solver was coupled to a three-dimensional Reynolds-averaged Navier-Stokes solver for the prediction of integrated stresses and strains on a rotor blade in forward flight. All major pieces of the 3D workflow were implemented and analyzed. The structural model was an idealized representation of a fully articulated UH-60A-like rotor. The aerodynamic model was identical to the UH-60A rotor. The primary focus of this work was on the 3D CFD/CSD coupled solution procedure. Two different types of 3D interfaces were developed and the simpler of the two implemented. The coupled airloads were compared with flight test data. The coupled 3D blade stresses and strains were studied for generic patterns typical of rotors in high speed forward flight. Based on this work the following key conclusions are drawn.

1. An integrated aeromechanical analysis with a high-fidelity 3D representation of the structure can indeed be carried out for helicopter rotors in forward flight. Dynamic stresses and strains resulting from aerodynamic loading can then be calculated without any reduced order approximation. Advanced hub types and blade shapes can then be modeled without any reduced order assumption.

2. The convergence of the (implicit) CSD solver requires dynamic stiffness to be updated at every time

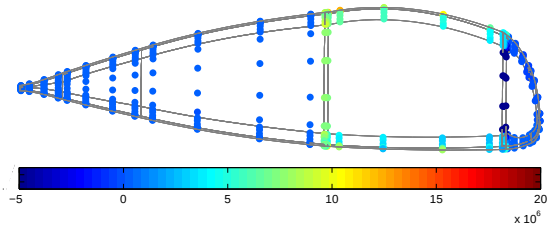

(a) Azimuth $\psi = 0°$

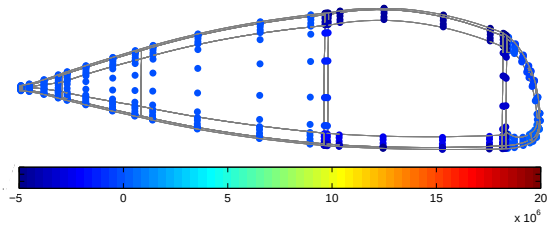

(b) Azimuth $\psi = 45°$

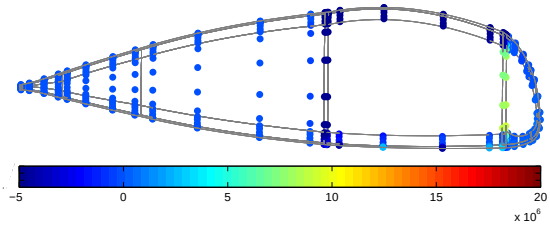

(c) Azimuth $\psi = 90°$

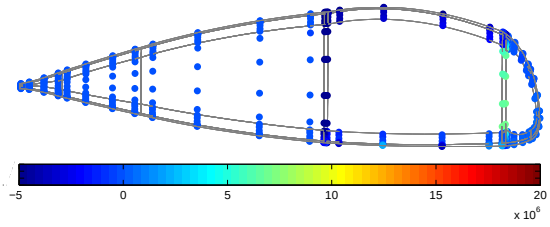

(d) Azimuth $\psi = 135°$

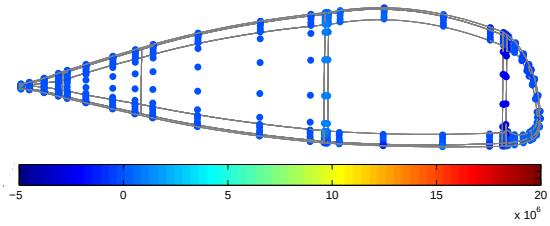

(e) Azimuth $\psi = 180°$

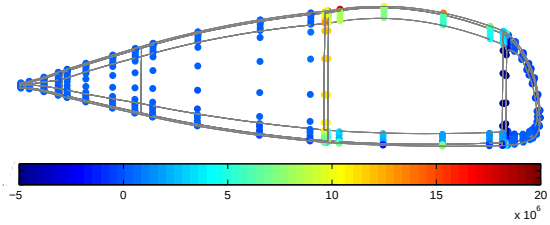

(f) Azimuth $\psi = 225°$

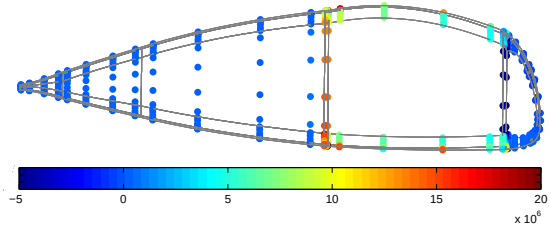

(g) Azimuth $\psi = 270°$

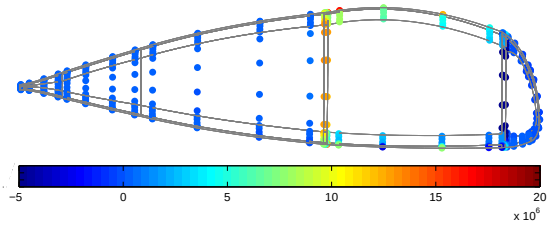

(h) Azimuth $\psi = 315°$

Figure 25: **Dynamic shear stresses in vertical direction (τ_{13}) predicted by 3D CFD/CSD analysis; 77% R station; colormap range: $-5 \times 10^6 - 20 \times 10^6$ N/m^2 (Pascal).**

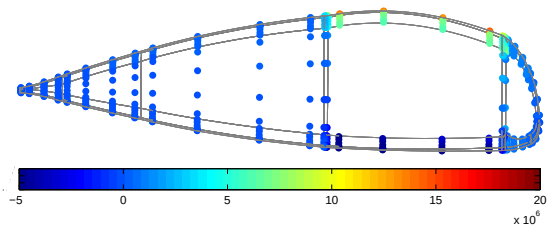

(a) Azimuth $\psi = 0°$

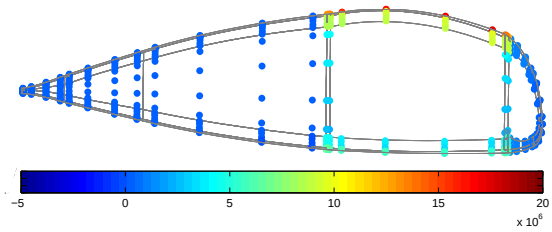

(b) Azimuth $\psi = 45°$

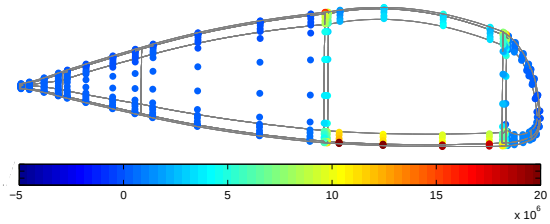

(c) Azimuth $\psi = 90°$

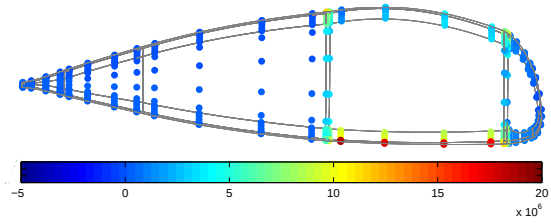

(d) Azimuth $\psi = 135°$

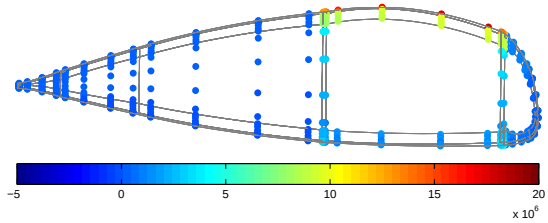

(e) Azimuth $\psi = 180°$

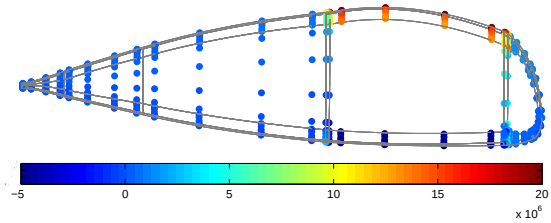

(f) Azimuth $\psi = 225°$

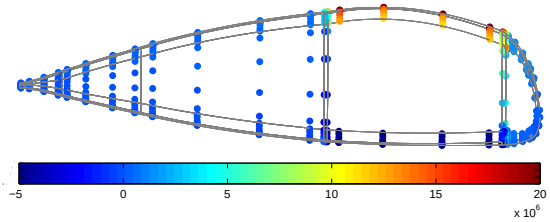

(g) Azimuth $\psi = 270°$

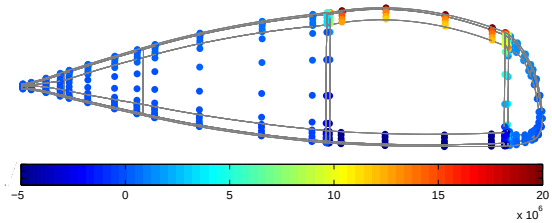

(h) Azimuth $\psi = 315°$

Figure 26: **Dynamic shear stresses in in-plane direction (τ_{12}) predicted by 3D CFD/CSD analysis; 77% R station; colormap range: $-5 \times 10^6 - 20 \times 10^6$ N/m^2 (Pascal).**

step. This is due to the strong non-linearities introduced by joints unified within 3D elements. For relatively large time steps sub-iterations are required — both for the accuracy of the response solution as well as for consistency of inertial loads with the response solution.

3. The time step is not dictated by the mesh resolution of the flexible 3D parts but rather by the non-linearities introduced by the joints. Thus a fine-mesh problem could be solved with the same stability and convergence behavior using the same time step as long as the trim conditions (joint motions) remained similar.

4. It is not essential that the finite element internal structure be populated in every detail for a nominal application of the analysis. The 3D interface can be made generic enough to accommodate an incomplete internal structure provided the primary load bearing pieces are in place. But a careful description of the material properties of these pieces are required so that the major blade offsets (E.A. and C.G.) are correctly located.

In the end we note that even though the CSD solver is parallel and scalable it was executed on a single processor in this study. The structural geometry, mesh, and material descriptions were representative of a realistic rotor but inexact and coarse. The exact patch force based level-II interface was developed but only the approximate level-I interface was implemented for integrated solution. A time integration procedure is an inefficient solution process to reach a periodic trim solution in a low-damped near resonance system like rotorcraft. These and other topics remain the subjects of future work.

REFERENCES

[1] Johnson, W., "A History of Rotorcraft Comprehensive Analyses," NASA/TP-2012-216012.

[2] Datta, A. and Johnson, W., "Three-dimensional Finite Element Formulation and Scalable Domain Decomposition for High Fidelity Rotor Dynamic Analysis," *Journal of the American Helicopter Society*, Vol. 56, (2), July 2011, pp. 1–14.

[3] Datta, A. and Johnson, W., "A Multibody Formulation For Three Dimensional Brick Finite Element Based Parallel and Scalable Rotor Dynamic Analysis," American Helicopter Society 66th Annual Forum Proceedings, Phoenix, AZ, May 11–13, 2010.

[4] Smith, M. J., Hodges, D. H., and Cesnik, C. E. S., "Evaluation of Computational Algorithms Suitable for Fluid-Structure Interactions," *Journal of Aircraft*, Vol. 37, (2), March–April 2000, pp. 282–294.

[5] Dowell, E. H. and Hall, K. C., "Modeling of Fluid-Structure Interaction," *Annual Review of Fluid Mechanics*, Vol. 33, pp. 445–490, January 2001.

[6] Datta, A and Johnson, W., "An Assessment of the State-of-the-art in Multidisciplinary Aeromechanical Analyses," American Helicopter Society Specialists' Conference on Aeromechanics, San Francisco, CA, January 23–25, 2008.

[7] Hou, G., Wang, J. and Layton, A., "Numerical Methods for Fluid-Structure Interaction — A Review," *Communications in Computational Physics*, Vol. 12, (2), August 2012, pp. 337–337.

[8] Bazilevs, Y., Takizawa, K. and Tezduyar, T. E., *Computational Fluid-Structure Interaction: Methods and Applications*, John Wiley & Sons Ltd, UK, 2013.

[9] Staruk, W., Chopra, I. and Datta, A., "Three-Dimensional CAD-Based Structural Modeling for Next Generation Rotor Dynamic Analysis," American Helicopter Society 70th Annual Forum Proceedings, Montréal, Québec, May 20–22, 2014.

[10] Blackford, L. S., Choi, J., Cleary, A., D'Azevedo, E., Demmel, J., Dhillon, I., Dongarra, J., Hammarling, S., Henry, G., Petitet, A., Stanley, K., Walker, D. and Whaley, R. C., *ScaLAPACK Users' Guide*, Society for Industrial and Applied Mathematics, Philadelphia, PA, 1997.

[11] Kuhl, D. and Crisfield, M. A., "Energy-conserving and Decaying Algorithms in Non-linear Structural Dynamics," *International Journal for Numerical Methods in Engineering*, Vol. 45, (5), June 1999, pp. 569–599.

[12] Bathe, K., "Conserving Energy and Momentum in Nonlinear Dynamics: A Simple Implicit Time Integration Scheme," *Computers and Structures*, Vol. 85, (7-8), April 2007, pp. 437–445.

[13] Strawn, R., "High-Performance Computing for Rotorcraft Modeling and Simulation," *Computing in Science and Engineering*, Vol. 12, (5), Sep-Oct 2010, pp. 27–35.

[14] Sitaraman, J., Potsdam, M., Wissink, A., Jayaraman, B., Datta, A., Mavriplis, D. and Saberi, H., "Rotor Loads Prediction Using Helios: A Multisolver Framework for Rotorcraft Aeromechanics Analysis," *Journal of Aircraft*, Vol. 50, (2), March 2013, pp. 478–492.

[15] Rohl, P. J., Dorman, P., Sutton, M., Kumar, D. and Cesnik, C., "A Composite Rotor Blade Structural Design Environment for Aeromechanical Assessments in Conceptual and Preliminary Design," American Helicopter Society 68th Annual Forum Proceedings, Forth Worth, TX, May 1–3, 2012.

[16] Farhat, C., Lesoinne, M. and Le Tallec, P., "Load and Motion Transfer Algorithms for Fluid/Structure Interaction Problems with Non-matching Discrete Interfaces: Momentum and Energy Conservation, Optimal Discretization and Application to Aeroelasticity," *Computer Methods in Applied Mechanics and Engineering*, Vol. 157, (1–2), pp. 95—114, April 1998.

[17] Choi, S., Datta, A., and Alonso, J. "Prediction of Helicopter Rotor Loads using Time-Spectral CFD and An Exact Fluid-Structure Interface," *Journal of the American Helicopter Society*, Vol. 56, (4), pp. 042001-1:15, October 2011.

[18] Tung, C., Caradonna, F. X., and Johnson, W. R., "The Prediction of Transonic Flows on an Advancing Rotor," *Journal of the American Helicopter Society*, Vol. 31, (3), July 1986, pp. 4–9.

[19] Datta, A., Sitaraman, J., Chopra, I. and Baeder, J., "CFD/CSD Prediction of Rotor Vibratory Loads in High Speed Flight," *Journal of Aircraft*, Vol. 43, (6), November-December 2006, pp. 1698–1709.